Finite Element Model Calibration of a Nonlinear Perforated Plate

David A. Ehrhardt[1]
University of Bristol, Bristol, UK, BS8 1TR

Matthew S. Allen[2]
University of Wisconsin-Madison, Madison, WI, 53706

Timothy J. Beberniss[3]
Wright-Patterson AFB, Dayton, OH, 45433

Simon A. Neild[4]
University of Bristol, Bristol, UK, BS8 1TR

This paper presents a case study in which the finite element model for a curved circular plate is calibrated to reproduce both the linear and nonlinear dynamic response measured from two nominally identical samples. The linear dynamic response is described with the linear natural frequencies and mode shapes identified with a roving hammer test. Due to the uncertainty in the stiffness characteristics from the manufactured perforations, the linear natural frequencies are used to update the effective modulus of elasticity of the full order finite element model (FEM). The nonlinear dynamic response is described with nonlinear normal modes (NNMs) measured using force appropriation and high speed 3D digital image correlation (3D-DIC). The measured NNMs are used to update the boundary conditions of the full order FEM through comparison with NNMs calculated from a nonlinear reduced order model (NLROM). This comparison revealed that the nonlinear behavior could not be captured without accounting for the small curvature of the plate from manufacturing as confirmed in literature. So, 3D-DIC was also used to identify the initial static curvature of each plate and the resulting curvature was included in the full order FEM. The updated models are then used to understand how the stress distribution changes at large response amplitudes providing a possible explanation of failures observed during testing.

Keywords: Nonlinear Normal Modes, Model Calibration, Geometric Nonlinearity

1. Introduction

Model calibration is an important step in the development of computational models that are representative of physical structures. In this context, there is a large suite of test and analysis approaches which use a structure's linear modes of vibration to guide the calibration of computational models [1, 2]. It is beneficial to note here that these techniques can be centered on a structure's linear modes of vibration using the complex mode definition or a more specific subset of complex modes that are called 'classical modes', 'undamped normal modes', or 'real modes', and here will be simply referred to as 'linear normal modes' (LNMs) of vibration [3]. In many instances, the LNMs, which are dependent only on the mass and stiffness distribution of a structure, are the preferred basis for comparison since damping is often not accounted for in the finite element model (FEM). When LNMs are employed in model calibration, the mass and stiffness can be updated such that they reproduce the measured natural frequencies and (real) mode shapes. However, characteristics of these LNMs such as amplitude invariance and orthogonality break down when a structure behaves nonlinearly. This has motivated many studies focused on expanding the definition of a structure's LNMs to include nonlinear behavior resulting in several definitions of what are termed *Nonlinear Normal Modes*.

[1] Post-Doctoral Research Assistant, Mechanical Engineering, david.ehrhardt@bristol.ac.uk
[2] Associate Professor, Engineering Physics
[3] Aerospace Structures Engineer, Aerospace Systems Directorate, Air Force Research Lab
[4] Professor, Mechanical Engineering

Two main definitions of nonlinear normal modes (NNMs) can be found in literature [4-7]. The first was developed by Rosenberg [4] for nonlinear conservative (i.e. un-damped) systems and limits a NNM to a *vibration in unison* of the nonlinear system. This definition was later extended to include *non-necessarily synchronous periodic motions* of the nonlinear system, and exploited by Kerschen et al [6] and Peeters et al [8] for the numerical computation of NNMs. Although using the conservative nonlinear equations of motion (computed using only mass and stiffness), this extended definition allows the inclusion of internal resonances which can lead to non-synchronous motions of the nonlinear system. It is worth noting this NNM definition has been generalized by Shaw [5], in which an NNM is defined as a two-dimensional invariant manifold in phase space extending the NNM concept to damped systems. The invariant manifold definition of an NNM has also been extended to include internal resonances by defining internally resonant NNMs as a $2m$-dimension invariant manifold where m is the number of modes retained for the definition of the invariant manifold [9-12]. This investigation focuses on the NNM definition used by Rosenberg, Vakakis, and Kerschen, and applies it to the numerical and experimental identification of NNMs of a continuous nonlinear system which is discritized using the underlying linear normal modes.

There have been several applications of undamped NNMs in the field of structural dynamics. For instance, NNMs have been used to provide insight to guide the design of nonlinear vibration absorbers [13] as well as a structure with tunable bending-torsion coupling [14]. NNMs have also been used to characterize FEMs of complicated, geometrically nonlinear structures aiding the creation of accurate nonlinear reduced order models [15, 16]. Kurt et al [17] numerically demonstrated the use of NNM backbone curves to guide the identification of nonlinear stiffness coefficients for a system with local nonlinearities. Of particular interest to this work, NNMs provide a tool to connect computational results with experimental measurements. For instance, NNMs have been used to correlate simulations [18] with experimental measurements [19, 20]. NNMs are an excellent tool for model calibration, because they provide a compact means for summarizing the measured or calculated nonlinear behavior of a system in the form of a frequency-energy (or frequency-amplitude) plot and the associated deformation shape. This investigation seeks to extend the use of NNMs to update parameters of a full-order geometrically nonlinear FEM.

The implementation of NNMs for the purpose of model calibration requires advanced techniques in their analytical or numerical calculation as well as their experimental measurement. Analytical techniques include the method of multiple scales [6, 7, 21, 22], normal forms [23], and the harmonic balance approach [24], but are typically restricted to structures where the equations of motion are known in closed form limiting their application to simple geometries and low order systems. Numerical methods have also been developed to calculate a system's NNMs without the approximations required in the analytical approaches [8] and have been used to compute the NNMs of relatively complicated structures [20]. These techniques have been extended to geometrically nonlinear finite element models (FEM) using an approach whereby the NNMs are calculated by coupling numerical continuation to transient dynamic simulation of full order FEM [25]. While numerical techniques are powerful, they are time consuming to implement for a large order FEM making application to iterative procedures (i.e. model calibration) difficult. Therefore in this investigation, the full order FEM is created and updated in Abaqus® and is used to create a nonlinear reduced order model (NLROM) following procedures discussed in [26]. The low order NLROMs are then used to examine NNMs with the use of the continuation routine presented by Peeters et al. [8].

Nonlinear normal modes can also be measured experimentally, but far less has been published in this area due to the difficulty of accounting for damping in the dynamic response of a structure, which is needed to isolate a NNM. Recent work has sought to identify NNMs using phase separation techniques relieving the need to cancel damping in the measurement of a NNM [27]. Alternatively using a phase resonance approach, NNM backbones have been identified from the damped dynamics of a structure using the free decay of a response initiated near a NNM solution [19, 28] or the stepped forced response using a multi-frequency input force [11]. The free decay results presented in [19, 28] have shown good agreement between calculated and experimentally identified NNMs; however, modal [11] and shaker-structure interactions [29] demonstrate that there is no guarantee a lightly damped transient will follow a NNM. Alternatively, the force appropriation technique used to initiate a free decay in [19] has been extended to identify a NNM by incrementally increasing the input force amplitude and tracking the phase lag criterion along a NNM backbone [11]. This stepped-force technique allows the implementation of multi-frequency inputs to account for damping changes with response amplitude and is used in this investigation.

The goal of this work is to propose and implement a model updating framework that can be used to accurately capture the linear and nonlinear dynamic response of geometric nonlinear structures. The first step in updating a

model is to decide which dynamic properties to measure and how to compare them between the model and experiment. In this work we focus on the physical parameters that have potential uncertainty and their effects on the global dynamics of the structure (i.e. LNMs and NNMs). Updates to the initial geometry, material properties, and boundary conditions are considered. Early measurements showed that a small difference between the FEM and actual geometry could change the nonlinear response considerably as discussed in literature [30, 31], so the initial shape of the plate was measured to sub-millimeter accuracy using static 3D digital image correlation (3D-DIC). The difference between the calculated and measured LNMs and NNMs were then used to update material properties and boundary conditions since LNMs and NNMs are closely tied to the physics of the real structure. The resulting models are shown to better represent the structure's linear and nonlinear dynamics. It is also shown that the changes made to the model based solely on its linear modal parameters may or may not improve the correlation of the model in nonlinear response regimes. Hence, it is critical to simultaneously consider both the linear and the nonlinear behavior of the system in the model updating process.

2. Background

2.1. Nonlinear Normal Modes

The concept of nonlinear 'normal' modes (NNMs) has seen much interest due to their usefulness in interpreting a wide class of nonlinear dynamics. While definitions are limited to conservative or weakly damped systems, NNMs provide an excellent summary of a mode of vibration's dependence on response amplitude. The reader is referred to [4, 6-8] for an in-depth discussion of NNMs in regards to their fundamental properties and methods of calculation. A summary of the methods used in this work is provided next.

Here, NNMs are numerically calculated using shooting techniques and pseudo arc-length continuation with step size control as implemented in NNMCont [8]. This method of calculation solves for periodic solutions of the nonlinear equations of motions, presented in Eqn. (1). Calculation begins in the linear response range and follows the progression of the system's dependence on the energy of the response. In Eqn. (1), [M] is the mass matrix, [K] is the stiffness matrix, and f_{nl} is the nonlinear restoring force that is a function of x. This method is capable of following the frequency-energy evolution around sharp changes in the NNM with the ability to track bifurcations, modal interactions, and large energy dependence of the frequency of vibration.

$$[\mathbf{M}]\{\ddot{\mathbf{x}}(t)\}+[\mathbf{K}]\{\mathbf{x}(t)\}+\mathbf{f}_{\mathbf{nl}}(\{\mathbf{x}(t)\})=0 \tag{1}$$

The NNMs of a structure can be measured with the use of force appropriation and an extension of phase lag quadrature as discussed by Peeters et al. in [18]. It was shown that an appropriated multi-point multi-harmonic force can be used to isolate the dynamic response of a structure on an NNM. The nonlinear forced response of a structure with viscous damping can be represented in matrix form by Eq. (2), where [C] is the damping matrix and $p(t)$ is the external excitation. As discussed before, an un-damped NNM is defined as a periodic solution to Eq. (1). So, when the input force is equal to the damping in a structure (Eqn. (3)), the dynamic response of a structure is on an NNM. Therefore, the forced response of a nonlinear system is on an NNM if the input force is equal to the structural damping for all response harmonics. As with linear force appropriation, the appropriated force can be simplified to single-point mono-harmonic components to produce a response in the neighborhood of a NNM, providing a practical application to experimental measurement. This simplification breaks down when the input force is not able to properly excite all modes in the response requiring careful consideration of input force location and harmonics needed. This technique has been experimentally demonstrated in [11].

$$[\mathbf{M}]\{\ddot{\mathbf{x}}(t)\}+[\mathbf{C}]\{\dot{\mathbf{x}}(t)\}+[\mathbf{K}]\{\mathbf{x}(t)\}+\mathbf{f}_{\mathbf{nl}}(\{\mathbf{x}(t)\})=\mathbf{p}(t) \tag{2}$$

$$[\mathbf{C}]\{\dot{\mathbf{x}}(t)\}=\mathbf{p}(t) \tag{3}$$

2.2. Perforated Plate Description

The structure under investigation is a circular perforated plate with rolled ends which is shown in Fig. 1a. A mechanical punch was used to create the circular perforations in a flat 16 gauge (1.52 mm thick) 409 stainless steel plate. The center each perforation was located at the vertex of an array of equilateral triangles with 10.16 mm long edges. Once this process was completed, the plate was formed around a 317.5 mm diameter mold with the excess trimmed so a lip of 24 mm remained. The plate was then welded to an 89 mm high cylinder made from a 14 gauge

(1.9 mm thick) 409 stainless steel plate that was cold rolled to the 317.5 mm diameter as shown in Fig. 1b. The final experimental setup shown in Fig. 1b is meant to simulate in situ conditions. The entire assembly was then bolted to a fixture with twelve 6.4 mm evenly spaced bolts attached to a rigid base. The linear natural frequencies and mode shapes were determined using a roving hammer test with 37 evenly spaced impacts and two light weight accelerometers mounted in the center of the plate.

The initial motivation of this work was to characterize nonlinear behavior of the fundamental mode of vibration at large response amplitudes as described in [11]; however, during testing an unexpected failure occurred in the center of the first plate tested (PP01) as shown in Fig. 1c in blue. A detailed image of the failure is shown in Fig. 1d, where the failed ribs are outlined in blue. This failure was repeated in the second plate tested (PP02). The region of this failure has been emphasized on the image of PP01 in Fig. 1c in green for comparison. A detailed image of the failure seen in PP02 is shown in Fig. 1e where the failed ribs are outlined in green. Although there is a slight difference in the location of the failure between the two plates (potentially from geometric differences discussed in Section 3.1), the failures occurred repeatedly and in an unpredicted location. The plate was driven near its first linear natural frequency, and the first mode shape exhibits peak stress near the circumference of the plate, not in the center. Using the measured LNMs and NNMs, a dynamically representative model will be created and will be shown to potentially explain this observed behavior.

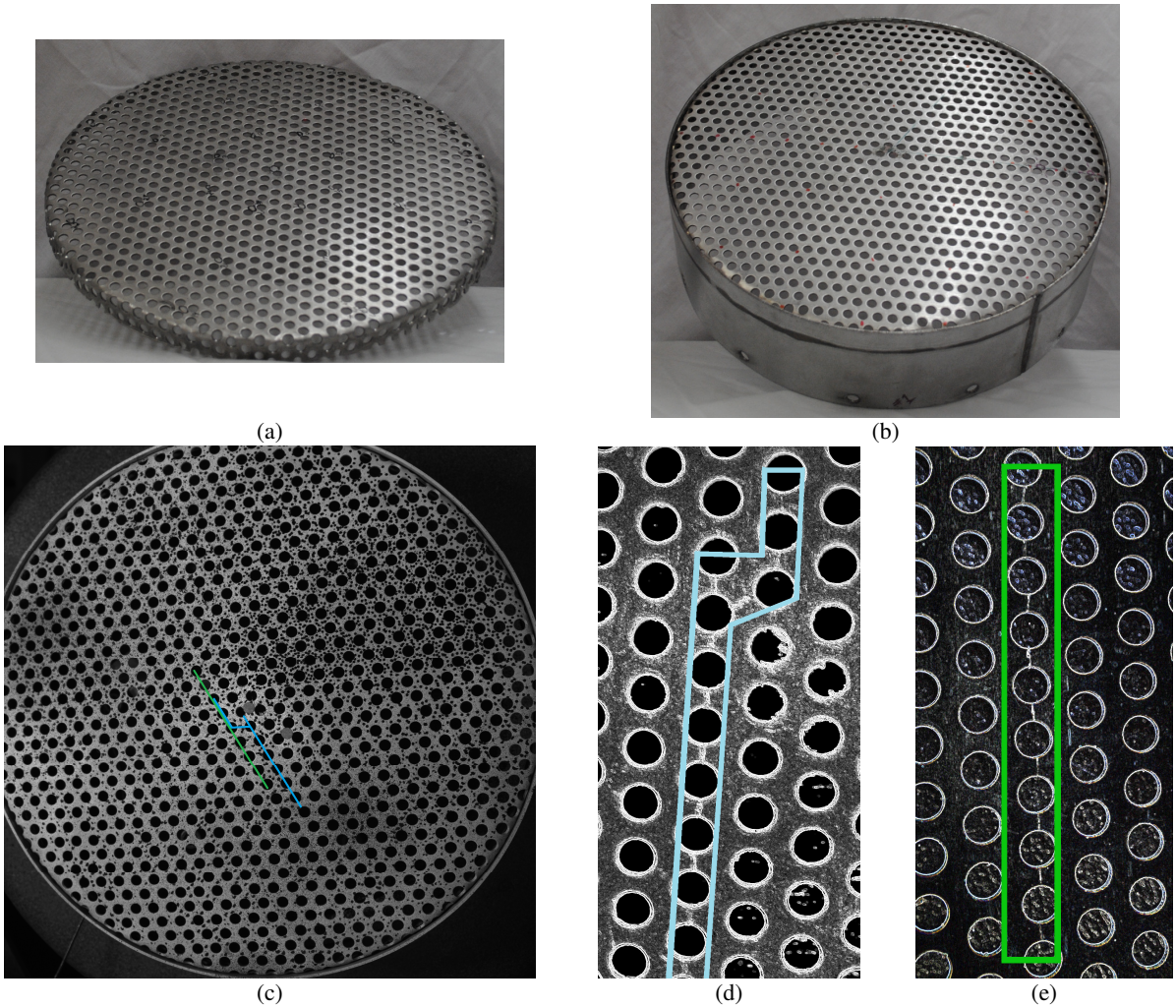

Figure 1: Experimental setup of the perforated plates. a) Perforated plate before welding into test configuration, b) Perforated plate welded into the supporting cylinder, c) Region of failure in both plates, and d & e) Detail of failures in both plates tested. The image has been modified using a threshold adjustment and edge detection algorithm in ImageJ [32] to emphasize the cracked ribs.

2.3. Model Description

In this investigation, an initial finite element model (FEM) was built using the nominal measured geometries of the perforated plate described in the previous section and is termed the Flat model. However, it is important to note that this model is perfectly flat but it includes that nominal radius of curvature of the plate around the circumference. The model is termed flat because the central region of the plate is modeled as flat when, in fact, this center region was later found to exhibit slight curvature. It is initially assumed that the welded boundary between the plate and steel cylinder provide fixed boundary conditions. Later this assumption was relaxed and springs were used to account for the in-plate stiffness of the support at the circumference of the plate. If a detailed representation of the stress distribution is needed, a very fine mesh would be required in order to model each of the perforations. However, Jhung and Jo [33] found that a perforated plate behaves dynamically identical to a non-perforated plate of the same dimensions, as long as the elastic properties are adjusted appropriately. Hence, a reduced elastic modulus and density were calculated based on the perforation geometry as detailed by Jhung and Jo. For the triangular perforation pattern of this plate a new elastic modulus of 168 GPa and density of 5120 kg/m^3 was found. The resulting meshed Abaqus® model is shown in Fig. 2, and has 1440 S4R shell elements.

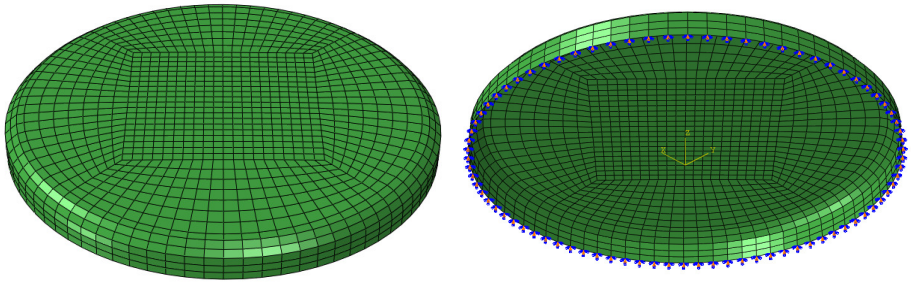

Figure 2: Meshed dynamically equivalent plate model

Although the resulting initial FEM (8886 degrees of freedom (DOF)) is substantially reduced when compared to the number of DOF needed to model the perforations (~400000 DOF), the initial FEM is still prohibitively large when simulating dynamic events. Therefore, a nonlinear reduced order model (NLROM) is created using the Implicit Condensation and Expansion (ICE) method [34-36]. In this method, the expected geometric nonlinearity due to large amplitudes of deformation is implicitly accounted for using nonlinear static solutions in Abaqus®. The nonlinear coefficients are determined using specific levels of applied modal forces and decomposing the resulting displacement onto the preselected modal basis for the NLROM and implicitly accounting for membrane effects. A system identification procedure is then utilized on the resulting restoring force/modal displacement relationship. The ICE method produces an N DOF system of equations in the modal domain as shown in Eqn. 4, where n is the number of modes included in the modal basis.

$$\ddot{q}_r + \omega_r^2 q_r + \sum_{i=1}^{n}\sum_{j=1}^{n} B_r(i,j) q_i q_j + \sum_{i=1}^{n}\sum_{j=1}^{n}\sum_{k=1}^{n} A_r(i,j,k) q_i q_j q_k = 0 \tag{4}$$

This type of NLROM should be adequate for this investigation since: 1) the focus of this investigation is near a single mode and 2) the nonlinear effects due to stiffness should dominate the geometric nonlinearity of this thin structure. The creation of NLROMs for the nominal dimensions of the plate has been discussed in [26] where it was shown that an accurate NLROM should include the first and sixth mode resulting in a 2-DOF representation of the structure. For this work, Eqn. 4 can therefore be expanded to a 2-DOF spring-mass system as shown in Eqn 5. In this context, it is beneficial to view the nonlinear behavior as a coupling between the first and sixth mode of vibration. Accordingly, in linear response regimes the system response remains uncoupled using the linear modes of vibration; however, in nonlinear response regimes, the system response now includes both the first and sixth mode. The 2-DOF NLROMs created using the ICE method are used to find NNMs of the structure by implementing continuation techniques discussed in [8] for a further comparison with experimentally measured NNMs.

$$\begin{aligned}\ddot{q}_1+\omega_{n1}^2 q_1+\alpha_1 q_1^2+2\alpha_2 q_1 q_2+\alpha_3 q_2^2+\gamma_1 q_1^3+3\gamma_2 q_1^2 q_2+\gamma_3 q_1 q_2^2+\gamma_4 q_2^3=0\\ \ddot{q}_2+\omega_{n2}^2 q_2+\alpha_2 q_1^2+2\alpha_3 q_1 q_2+\alpha_4 q_2^2+\gamma_2 q_1^3+\gamma_3 q_1^2 q_2+3\gamma_4 q_1 q_2^2+\gamma_5 q_2^3=0\end{aligned} \quad (5)$$

2.4. Modeling Considerations

Although the plate is a relatively simple structure compared to the vehicle it is attached to, validating the FEM with experimental measurements involves some engineering judgment and physical insight to the inherent uncertainty of the physical assembly. Uncertainties in initial geometry, material properties, and boundary conditions are expected to dominate errors between the model and experimental structure. In Figure 3, the areas of potential uncertainty are shown in orange: K_R represents the stiffness of the boundary in the radial direction, and the orange line represents the initial geometry. The starting point for the model updating procedure uses the nominal geometry (shown in black), nominal material properties (as predicted by [33]), and fixed boundary conditions ($K_R = \infty$). Variations in the initial geometry (shown in orange) are taken into account with the use of full-field static 3D-DIC coordinate measurements of the plate surface. The remaining error between the model and measurement is accounted for by tuning the modulus of elasticity and boundary conditions during the two updating steps as detailed in the next section. The reduced density was not updated since it can be computed from the geometric properties of the perforations (i.e. size of hole and count) and hence should be quite accurate. On the other hand, the effective modulus is dependent on any residual stresses from the addition of perforations, imperfections of the perforation location geometry, and curvature from the forming processes. Similarly, the stiffness, K_R, has potential variation due to the flexibility of the cylinder to which the perforated plate is welded. All six DOFs at the boundary were initially considered; however, it was found that only K_R is important and is presented in this work.

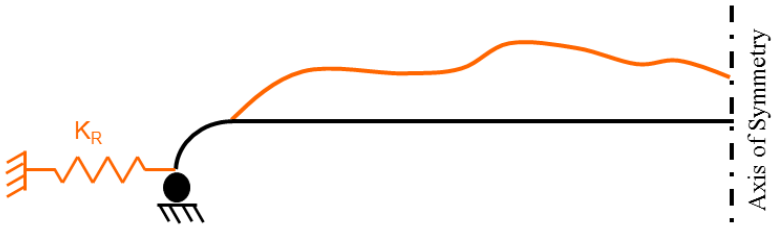

Figure 3: Boundary Condition Schematic

3. Updating Results

The initial full order FEM is built assuming nominal geometric and material properties, and fixed boundary conditions. There are two updating steps performed on the initial nominal model based on experimental data as detailed in Fig. 4. In Update 1, the initial geometry of the model is changed to the geometry measured with 3D-DIC. Next, the modulus of elasticity, E, is updated based on the predicted linear natural frequencies. In Update 2, the boundary stiffness, K_R, is updated using the frequency at the transition from spring softening to spring hardening observed in the dynamic behavior of the NNM.

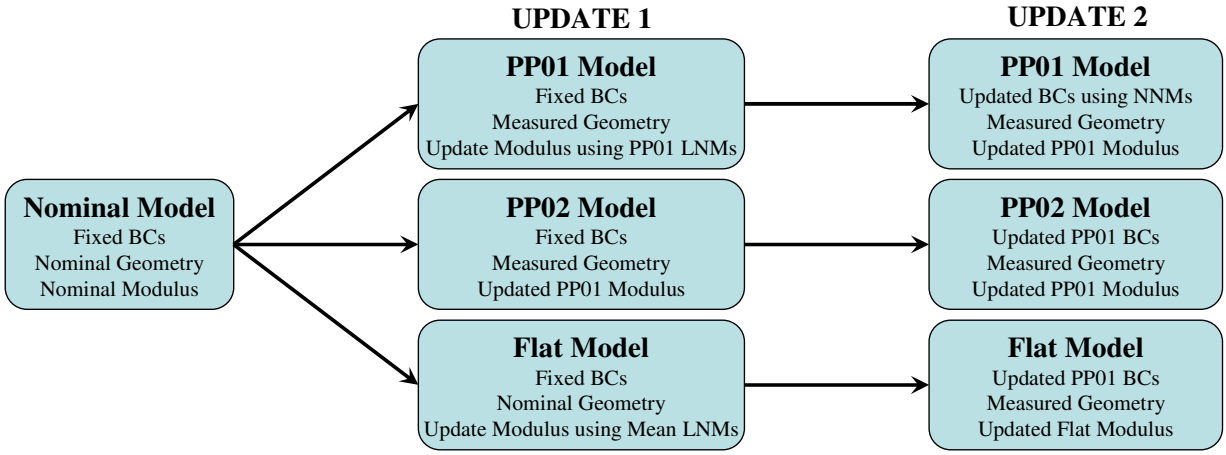

Figure 4: Model updating flow chart

The model was updated using a cost function to weigh the error in each frequency of interest on a percentage basis as presented in Eqn. (6). For Update 1, the frequencies of interest are the linear natural frequencies, and for Update 2, the frequency of interest is the frequency at the transition from spring softening to spring hardening. The updating was achieved by using finite differences to compute the Jacobian with respect to each of the parameters $\mathbf{p}=[E, K_R]$.

$$g(\mathbf{p}) = \sum_{r=1}^{N} \left(\frac{f_{r,FEM}(\mathbf{p}) - f_{r,ex}}{f_{r,FEM}(\mathbf{p})} \right) \tag{6}$$

3.1. Initial Conditions and Linear Updating

Although subjected to similar mechanical loads during manufacturing, each plate will have variations in the final geometry and the results will show that these must be identified to obtain an accurate model. Using static 3D-DIC, the initial geometry of the surface of each plate is measured resulting in a dense point cloud describing the shape. It is assumed that the lip of the plate (i.e. the edge welded to the cylinder shown in Fig. 1) remains near circular and would have little effect on the final structural response since the primary deformation is along the Z-axis (as defined in Fig. 5). The surface measurement is applied to the FEM using bi-harmonic interpolation. Two FEM are created which describe the shape of PP01 and PP02 as seen in Fig. 5. It is interesting to note that each plate shows a slightly different asymmetry in the deformation. This is most noticeable in the XY plot of the curvature (Figs. 5a and 5c) where the largest deformation (dark red) is skewed in the positive Y direction and the negative X direction. For comparison, the peak curvature observed for PP01 (3.73mm) is lower than the peak curvature observed for PP02 (4.84mm) resulting in slightly different natural frequencies for each FEM once the measured curvature was applied to the mesh, as seen in Tab. 1.

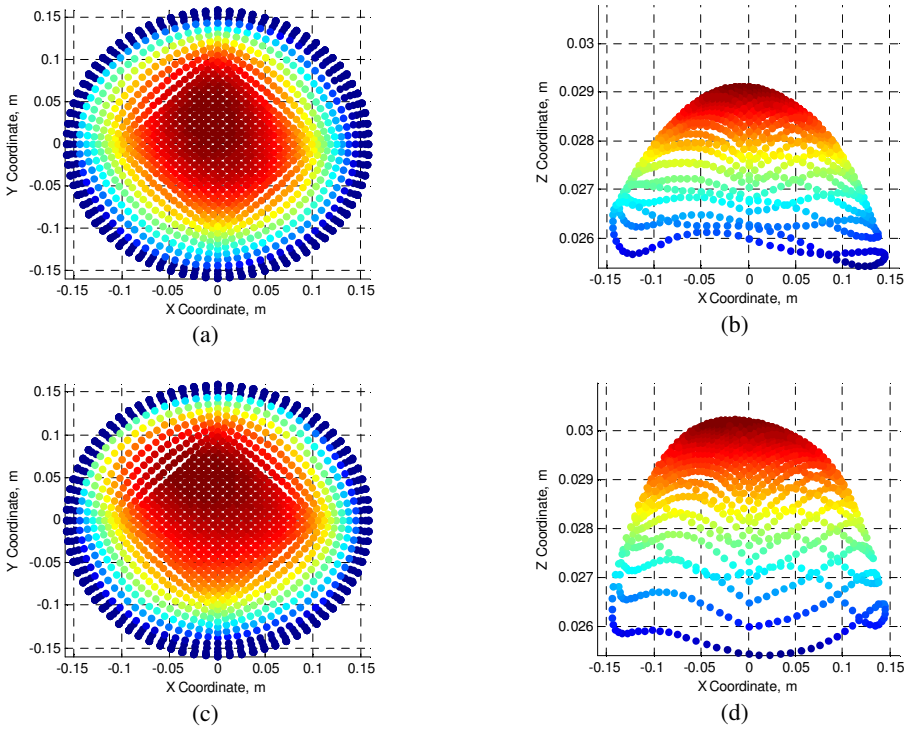

Figure 5: Initial geometry of each plate measured with 3D digital image correlation. a-b) PP01, c-d) PP02

Since there are several areas of uncertainty between the model and the experiment, there is potential for the model calibration process to deliver non-physical results or lead to a non-optimal result. Therefore, in this investigation, we will use experimental and numerical data from PP01 to guide each model calibration step, and blindly apply the resulting values to PP02 to gain insight into the robustness of the model calibration. In addition to the two models created with the measured geometry of PP01 and PP02, a nominal (Flat) model is created to demonstrate the

difference in nonlinear behavior. During the model calibration of the Flat model, an average between the PP01 and PP02 experimentally identified natural frequencies is used to guide the model calibration steps in an attempt to produce the 'best' flat model that could be used for both plates.

Table 1 provides a summary of the first 10 natural frequencies for the results obtained during Update 1 of the model calibration. Using the material properties previously defined as a starting point, the Flat (NUM 1) model was created to reduce the percentage error between the measured natural frequencies. Several combinations of physical parameters were used to update the Flat model based on the expected experimental uncertainties (i.e. boundary conditions and modulus of elasticity). The best updated Flat (NUM 1) model is presented in Tab. 1, where K_R was not changed (i.e. boundary was infinitely stiff) and the modulus of elasticity decreased to 132 GPa (decrease of 21%). While some linear modal frequencies are captured accurately, the resulting model does not appear to capture the linear natural frequencies in Modes 1, 3, and 9, as shown in Tab. 1. An additional compariosn is made between the calculated and measured mode vectors using the modal assurance crieterion (MAC) [37]. The MAC value between the resulting Flat model and experimentally measured PP01 mode shapes for Modes 1, 3, and 9 show a good agreement. This information provides an indication of the distributed nature of the error (i.e. geometry of the structure) which would preserve the distribution of mass and stiffness thereby minimally changing the mode shapes.

The same procedure was applied to the PP01 (NUM 1) model to reduce the percent error between the measured natural frequencies for PP01 (EXP). The best updated model produced a reduction in the modulus of elasticity to 96 GPa (decrease of 43%) with no change in K_R. The resulting update brought the errors between natural frequencies within 6%, and had varying effects on the MAC values. The reduction in modulus for PP01 (43%) compared with the Flat model (21%) emphasizes the importance of the initial curvature in the updating process when examining the effective modulus. The resulting modulus update for PP01 was then blindly applied to the PP02 (NUM 1). Both PP01 and PP02 models show better agreement in the first ten natural frequencies when compared with the Flat model as seen in Tab. 1 leading to the conclusion that the model is a good representation of the experimental setup after simply updating the elastic modulus (decrease of 43%) and curvature (3-5mm over a diameter of 300mm). The updating results for PP02 demonstrated a larger average frequency error but good agreement in all MAC values. Since only minor differences are observed between the mode shapes of PP01 and PP02, only the modes shapes of the experimentally measured PP01 and updated PP01 model are presented in Fig. 6. Here a good agreement is seen between both sets of modes.

In the absence of a measurement of the initial curvature, the updated Flat model may be all that is available to understand the dynamics of the structure. Since the mode shapes of the measurement and flat model match well, one may be tempted to factor in the frequency difference in any further analysis and stop updating at this point; however, the flat model misses important nonlinear characteristics of the dynamic response as discussed in Section 3.3.

Table 1: Perforated Plate Correlation Results

Model	Flat				PP01				PP02			
Mode #	f_n, Hz, EXP AVG	f_n, Hz, NUM 1	Mean % Err.	MAC	f_n, Hz, EXP	f_n, Hz, NUM 1	% Err.	MAC	f_n, Hz, EXP	f_n, Hz, NUM 1	% Err.	MAC
1	213.75	154.01	27.95	0.980	205.36	202.26	1.51	0.990	222.13	210.77	5.11	0.983
2	339.18	319.52	5.80	0.870	327.84	328.86	-0.31	0.983	350.51	350.80	-0.08	0.976
3	356.80	319.52	10.45	0.835	348.65	352.10	-0.99	0.955	364.95	363.78	0.32	0.990
4	506.18	527.64	-4.24	0.903	489.17	512.93	-4.86	0.887	523.19	548.75	-4.88	0.912
5	526.68	528.62	-0.37	0.945	510.23	528.16	-3.51	0.972	543.12	564.80	-3.99	0.857
6	571.87	604.38	-5.68	0.945	572.63	559.94	2.22	0.900	571.12	573.49	-0.41	0.869
7	711.78	777.36	-9.21	0.930	697.90	736.59	-5.54	0.844	725.66	783.02	-7.90	0.903
8	715.14	777.36	-8.70	0.906	699.95	737.37	-5.35	0.779	730.33	787.95	-7.89	0.897
9	796.45	922.05	-15.77	0.933	814.12	821.08	-0.86	0.851	778.78	840.18	-7.88	0.820
10	852.27	922.05	-8.19	0.941	827.68	832.57	-0.59	0.854	876.85	849.89	3.07	0.867

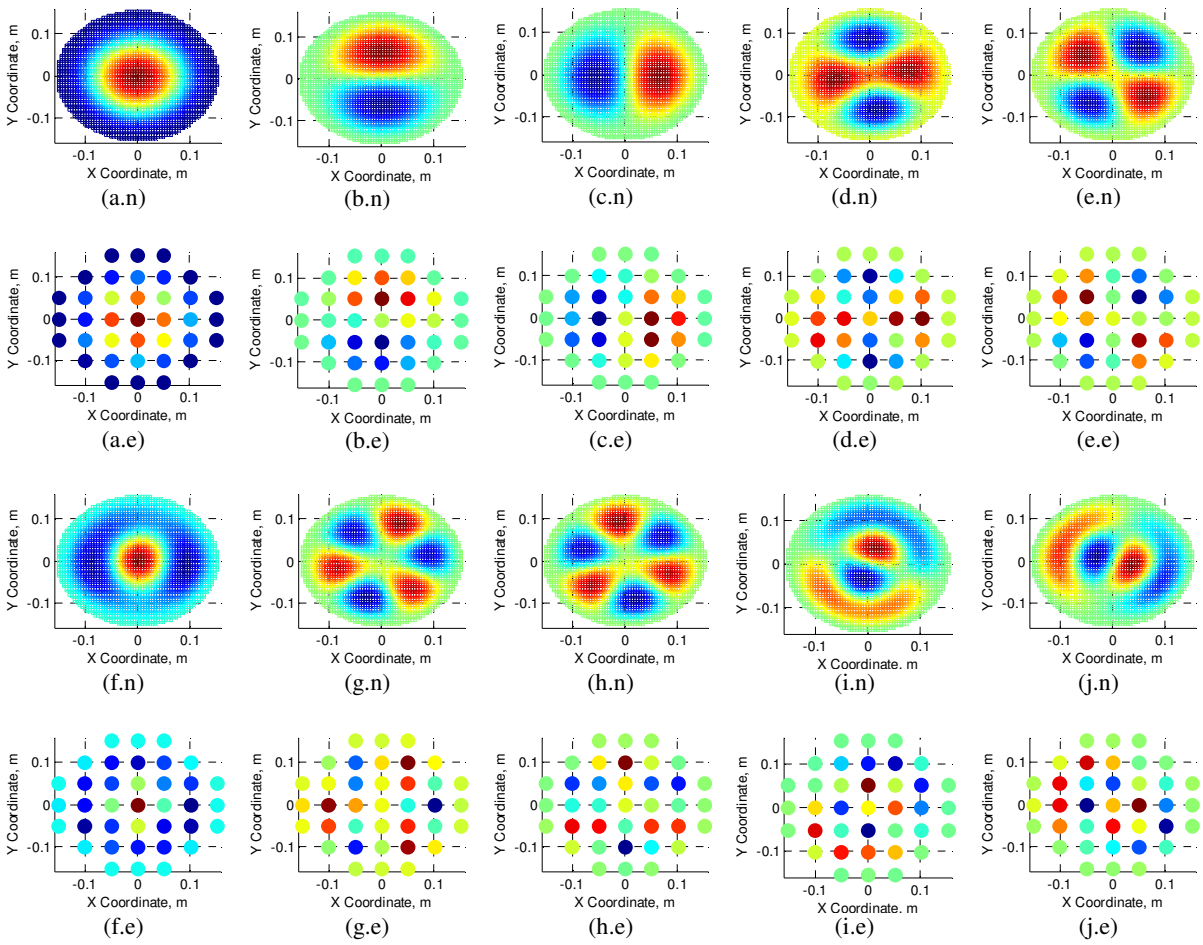

Figure 6: Numerical (X.n) and experimental (X.e) mode shapes of the first 10 modes for the updated PP01. Modes 1-10 correspond to a-j, respectively.

3.2. Examination of Experimental NNM Backbone Curves

The NNMs for the perforated plate can be obtained experimentally by exciting the system with a sinusoidal input and adjusting the frequency and amplitude until the phase quadrature is satisfied, as described in [11]. In this investigation, a mono-frequency base excitation was applied to the structure as the phase was tracked between the input voltage to the shaker and the response velocity at the center of the plate, and once a point was found the amplitude of the input voltage was increased to follow the NNM to higher amplitudes. The resulting experimental NNM for PP01 is shown in Fig. 7a. For the experimental setup, we were able to capture 12Hz of spring softening before 4.5Hz of spring hardening. Above this level of response, PP01 failed as previously described. At a higher level of response amplitude along the NNM (i.e. at the point labeled 'Point 1' in Fig. 7a), a multi-frequency response is observed in Fig. 7b, although only mono-frequency voltage was used to drive the shaker, the measured base motion also shows higher frequency content bringing into question the validity of the mono-frequency excitation. To provide context, the amplification factor from the base motion to the response at the center of the plate at $1*f_{in}$ is 360 (i.e. 360 times more response is observed than base motion) and is 328 at $3*f_{in}$ revealing that the velocity of the 3rd harmonic is almost as strong as the first. The large amplification factor almost 10Hz from the 1st linear mode of vibration and 7Hz from the 6th linear mode of vibration (closest to $3*f_{in}$) provides an indication to the level of nonlinearity in the response of the structure. An examination of the phase between the response of the plate at $1*f_{in}$

and 3*f_{in} (4.43deg compared to 0 degrees for perfect NNM measurement) provides an indication of how well the NNM of the structure is captured at the largest amplitude of deformation.

In this experimental setup we had the benefit of measuring full-field dynamic displacements using high speed 3D digital image correlation from a previous setup [38] capturing images at 4000 Hz. The full-field measurement of the plate provides an indication of which linear modes of vibration are participating in the multi-frequency dynamic response shown in Fig. 7b. A qualitative examination of the physical deformation at 1*f_{in} (Fig. 7c) reveals a distinctive Mode 1 shape. Similarly, at 2*f_{in} (Fig. 7d) a combination of Mode 1 and Mode 6 is observed, whereas at 3*f_{in} (Fig. 7e) only a Mode 6 shape is observed. Finally, at 4*f_{in} (Fig. 7f) a distinctive Mode 10 shape is observed, although peak velocity is two orders of magnitude smaller than the fundamental. This measurement shows a strong participation of Mode 1 and Mode 6 in the dynamic response at 1*f_{in} and 3*f_{in} (i.e. the dominant frequencies) giving a good indication of the important modes participating at this response level. The fact that Mode 6 is shown to be important in the measured nonlinear response of the plate reinforces previous numerical studies [26]. However, a deeper understanding of how Mode 6 participates in the dynamic response is sought and will be discussed in the next section.

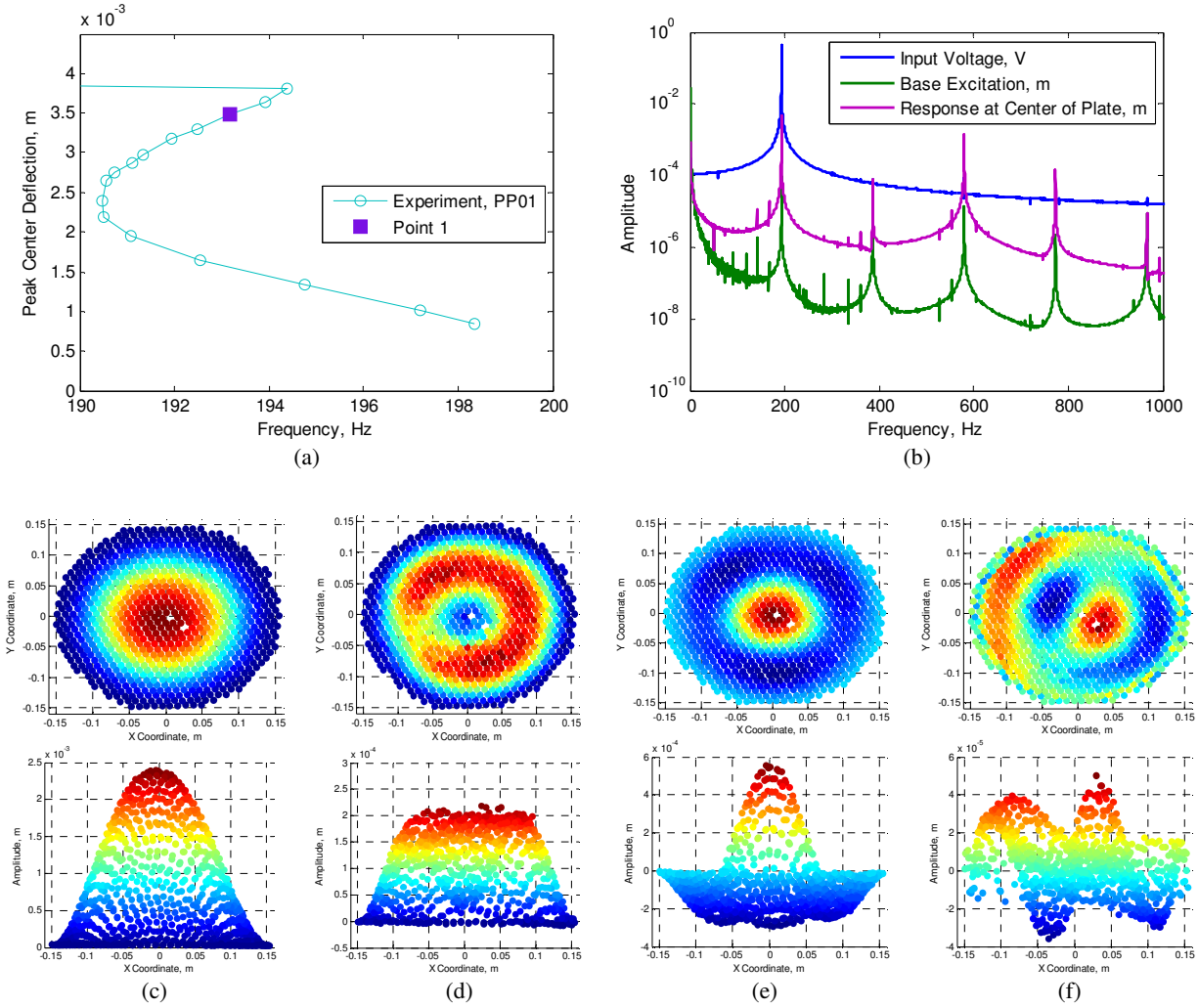

Figure 7: Experimental NNM backbone curve. a) Peak displacement vs. frequency, b) FFT of input (acceleration and voltage) and response velocity, c) Deformation of Point 1 at 1*f_{in}, d) 2*f_{in}, e) 3*f_{in}, and f) 4*f_{in}

3.3. 2DOF NLROMs and Comparison with Experimental Results

From a previous numerical study it has been shown that Mode 6 must be included in the formation of the NLROM to predict the nonlinear behavior of the plate [26], which is also confirmed in the measured NNMs shown in the previous section. Therefore, 2-DOF NLROMs are created using Mode 1 and Mode 6 as a basis for the three models created in this work. The inclusion of Mode 6 to the NLROM requires consideration of the level of the maximum static deflection each mode undergoes to implicitly account for membrane effects and build the NLROM. It was previously found that using a deformation for Mode 1 and Mode 6 of 1*thickness and 0.25*thickness of the plate in the static load cases applied to the FEM to resulting in the creation of a converged NLROM. The first NNM of all models are compared with the measured NNM of PP01 and PP02 in Fig. 8. It is observed that the general characteristics of the NNM are captured (i.e. spring softening to hardening), but there is a discrepancy to the amplitude of deflection as well as frequency where hardening begins and the amount of softening observed in the NNM for the PP01 and PP02 models. It is of interest to note that the Flat model completely misses the nonlinear behavior predicted and observed in the perforated plate and only shows spring hardening behavior. While it is well known that curved structures exhibit softening behaviors that are not observed in flat structures [30, 31, 39], all three models included the curvature around the perimeter, and it was not initially apparent that the small curvature in the central section would have such an important effect on the nonlinear dynamics of the plate.

More insight to the dynamic response of the plate can be gained by examining the time series of a period of the predicted and measured response at different amplitudes. In Fig. 8b-f the full field displacement is projected onto the mode shapes which have been normalized to the peak z-deflection to preserve the relative scale of the deformation of each mode in the physical response. The time series of Mode 1 (dash) and Mode 6 (dot) are shown for the two experimental measurements and the three models near a peak deflection of 0.1mm (purple), 0.2mm (green), and 0.3mm (orange) in Figs. 8b-f. In Fig. 8b, the experimental time series of the measured NNM at these points for PP01 is shown. As expected, Mode 6 becomes more pronounced at higher levels of response amplitude and primarily oscillates at three times the fundamental frequency. It is interesting to note that at all levels an asymmetry is observed in the amplitude of the peak deformation of the time series of both modes. A similar behavior is observed in the PP02 experimental results shown in Fig. 8c; however, a lower amplitude of Mode 6 is at a similar level of peak center deflection. A comparison of the experimental results from PP01 (Fig. 8b) and the numerical results of PP01 (Fig. 8d) reveals an over prediction of the participation of Mode 6 at higher levels of response amplitude. This provides an indication of missing or inappropriately accounted for coupling between Mode 1 and Mode 6. Also, the phase relationship between Mode 1 and Mode 6 is 180 degrees different for the model while the experiment predicts an in-phase behavior. The phase difference can be traced back to the phase of the calculated linear modes when compared to the measured modes of vibration. The NNM of the Flat model (Fig. 8f) shows minimal participation of Mode 6 in the period of the response emphasizing again the important difference observed in the Flat model. At this point it is difficult to determine the next step in the model updating procedure, but a consideration of the experimental setup points to a potential need to relax the boundary conditions due to the assembly of the perforated plate.

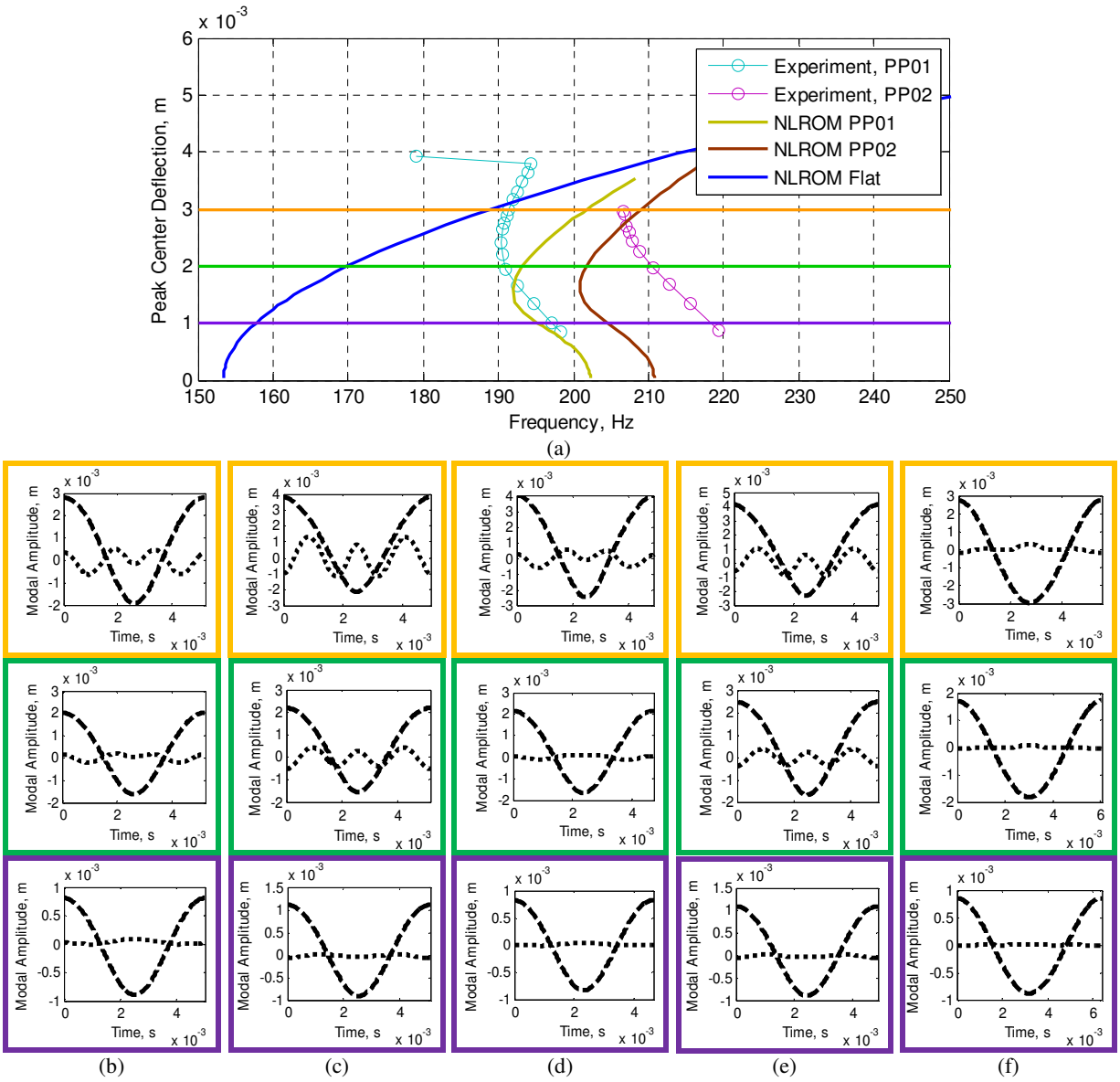

Figure 8: Comparison of the NNMs experimentally measured and numerically calculated from the FEMs after Update 1. a) Frequency-amplitude plot and time series results for Mode 1 (dash) and Mode 6 (dot) at 0.1mm (purple), 0.2mm (green), and 0.3mm (orange) deflections for b) PP01 Experiment, c) PP01 Model, d) PP02 Experiment, e) PP02 Model, and f) Flat model.

3.4. Updating Based on Nonlinear Normal Mode Backbone Curves

Using the NNM of PP01, the difference between the measured and predicted peak deflection at the center of the plate at the 'turning point' from spring softening to spring hardening is reduced. Using a forward difference gradient based optimization leads to a reduction in boundary stiffness to K_R = 650000 N/m. This boundary condition is blindly applied to PP02 and the Flat model. Both curved models show a better agreement with the experimentally measured NNMs as seen in Fig. 9a. The time series of PP01 (Fig. 9b) also shows better agreement with the experimentally measured time series of PP01 (Fig. 8b). The relaxation of the boundary conditions improves the amplitude of Mode 6, and the phase between Mode 1 and Mode 6. The updated boundary conditions applied to the PP02 model (Fig. 9c) which shows a better representation of the contribution of Mode 6 to the dynamic response, but does a worse job predicting the asymmetry observed in Mode 1 when compared with the experimental results previously presented in Fig. 8c. It is interesting to note that the reduction in boundary conditions shifted the asymmetry of the modes in the time domain for the Flat model (Fig. 9d) toward the measured asymmetry. While the

updated models do not provide an exact comparison with experimental results, the resulting NLROMs describe the behavior of the perforated plates well.

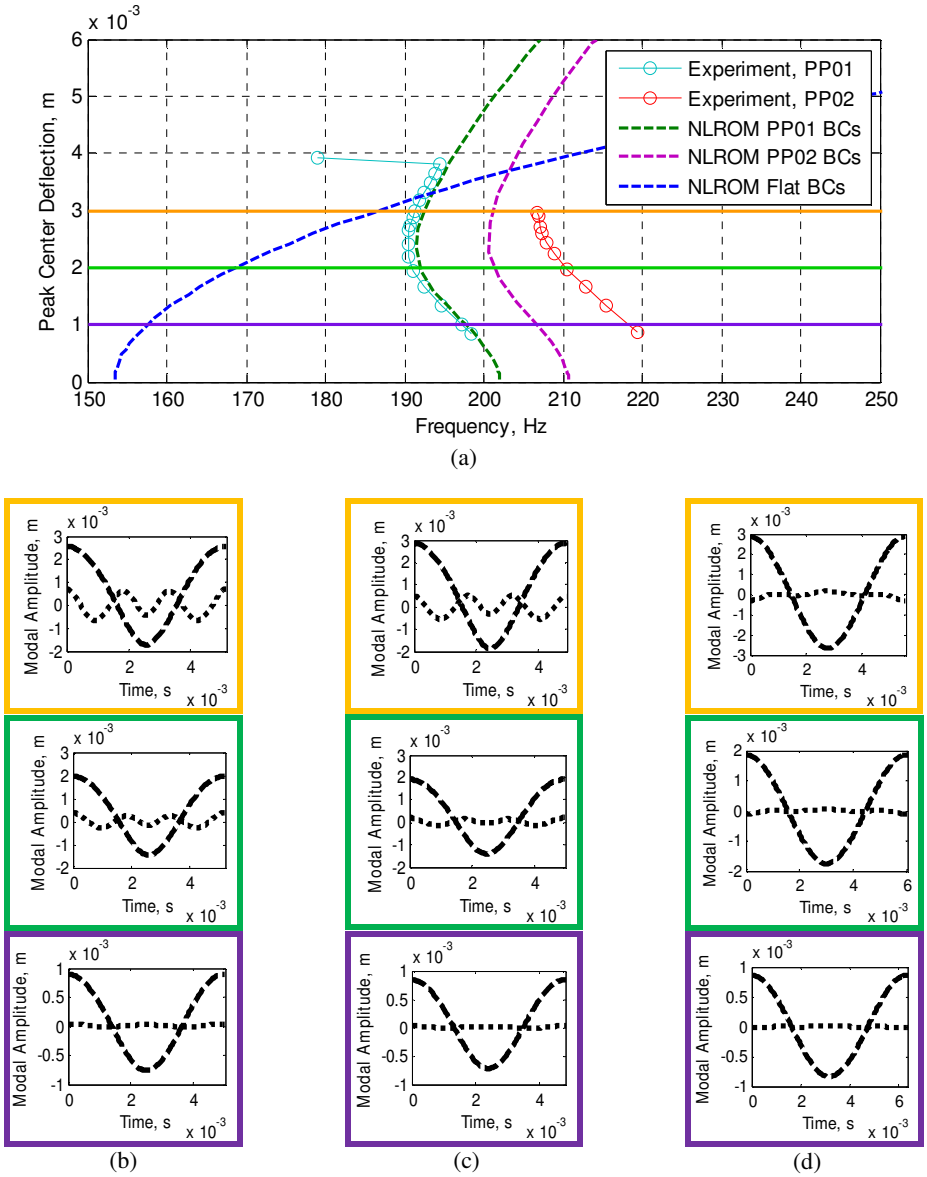

Figure 9: Comparison of the NNMs numerically calculated from the FEMs after Update 2. a) Updated NNMs and time series results at 0.1mm (purple), 0.2mm (green), and 0.3mm (orange) deflections for b) PP01 Model, c) PP02 Model, and d) Flat model

So as not to invalidate all previous updating results, the relaxation of the boundary conditions should have limited effect on the linear natural frequencies. At this point it is beneficial to revisit a comparison between the linear natural frequencies of the NLROMs and the experimental measurements. With the relaxation of the boundary conditions, the natural frequencies of all models show minimal change. This emphasizes that the boundary conditions were not fully perturbed during linear testing and was missed in the first updating step. A better representation of the perforated plates could be found by using both PP01 and PP02 results during the updating providing a more optimum result; however, the model updating steps have shown a level of robustness since the primary focus has been on creating the best model to match PP01.

Table 2: Frequency results from boundary condition update

Model	Flat			PP01			PP02		
Mode #	f_n, Hz, EXP AVG	f_n, Hz, NUM 3	% Err.	f_n, Hz, EXP	f_n, Hz, NUM 3	% Err.	f_n, Hz, EXP	f_n, Hz, NUM 3	% Err.
1	213.75	153.45	28.21	205.36	202.03	1.62	222.13	210.71	5.14
2	339.18	317.43	6.41	327.84	327.89	-0.01	350.51	350.48	0.01
3	356.80	317.43	11.03	348.65	351.37	-0.78	364.95	363.47	0.41
4	506.18	524.51	-3.62	489.17	511.94	-4.66	523.19	548.16	-4.77
5	526.68	525.87	0.15	510.23	526.34	-3.16	543.12	564.36	-3.91
6	571.87	601.63	-5.20	572.63	558.33	2.50	571.12	572.31	-0.21
7	711.78	774.59	-8.82	697.90	735.73	-5.42	725.66	782.54	-7.84
8	715.14	774.59	-8.31	699.95	737.8	-5.41	730.33	787.65	-7.85
9	796.45	924.26	-16.05	814.12	824.29	-1.25	778.78	837.55	-7.55
10	852.27	924.26	-8.45	827.68	835.38	-0.93	876.85	847.43	3.36

3.5. Stress Distribution of the Final Updated Models

Using the updated NLROMs, we can now explore potential causes of the failures observed in the experimental testing of PP01 and PP02. Before examining the stress distribution throughout increasing nonlinear responses, it is beneficial to note that a circular flat plate with fixed boundary conditions undergoing distributed loading is expected to have the highest stresses near the clamp. However, small differences in the boundary conditions will reduce edge stresses while increasing the deflection and stresses at the center of the plate [40]. The plates presented here show an interesting combination of these effects due to the changes in the boundary conditions we have implemented as well as internal forces predicted in the plates. It was demonstrated in Fig. 7, that along the NNM backbone a dominant interaction with Mode 6 is observed at $3*f_{in}$ with secondary effects observed at $2*f_{in}$ and $4*f_{in}$. Since the failures observed were in the center of the plate, the modal interaction is thought to change the stress distribution at higher response amplitudes so a 'hot spot' forms near the center of the plate.

This is demonstrated by reconstructing the displacement and stress in the plate at various points along the NNM. To do this, Mode 1 and Mode 6 are superimposed and it is also important to use the expansion procedure outlined in [35] to account for in-plane stretching that is captured implicitly in the ICE method. This deformation is then applied to the structure using a nonlinear static analysis in Abaqus®. The internal stresses due to the predicted in- and out-of-plane deformations are resolved within the analysis. Plots of the peak stress observed over a period of the response at four levels of deformation along the NNM are shown in Fig. 10 for the three updated models. For the flat plate (Fig. 10d) the low amplitude deformation (purple) shows a high von Mises stress at the center and edge of the plate. At higher levels of deformation (blue to red) the stiffening from in-plane stretching becomes more apparent as the stress concentrates near the edge of the plate. For PP01 (Fig. 10b) and PP02 (Fig. 10c), the von Mises stress is highest at the edges for low amplitude of deformation (purple). At higher levels of deformation (blue to red), the Mode 6 interaction concentrates the highest level of stress just offset of the center of the plate forming a 'hot spot'. The location of this larger stress corroborates the failures observed in the experiment highlighting the importance of updating the FEM to account for the seemingly insignificant curvature of the center portion of the plate and correctly accounting for the boundary stiffness.

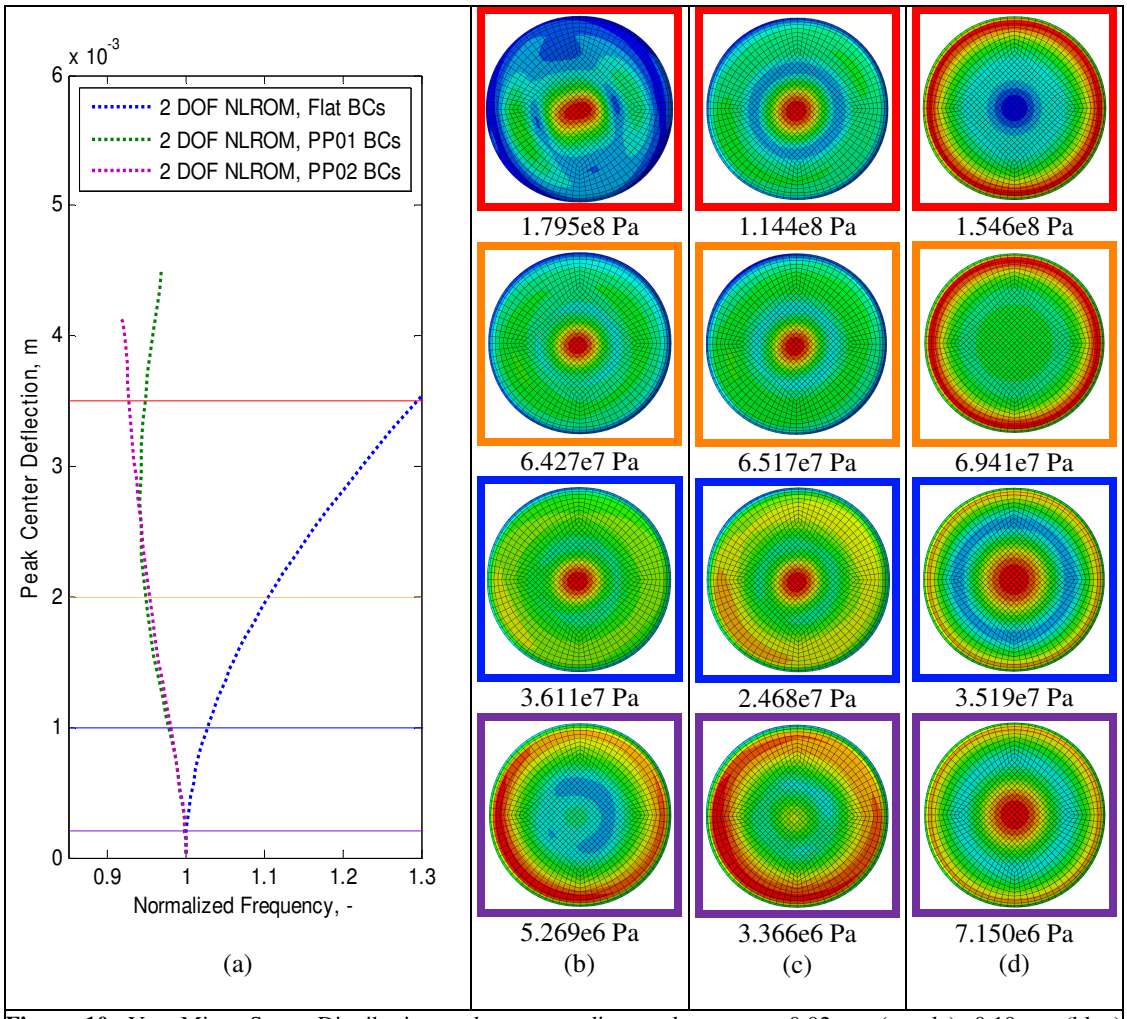

Figure 10: Von Mises Stress Distribution and corresponding peak stress at 0.02mm (purple), 0.10mm (blue) 0.20mm (orange), and 0.35mm (red) deflections along the NNM for the b) Flat model, c) PP01, and d) PP02.

4. Conclusions

This work has explored the use of NNM backbones as a metric for finite element model calibration in nonlinear response regimes for two axi-symmetric perforated plates. Full field measurements and previous numerical work has shown the importance of the coupling between mode 1 and mode 6 at larger response levels. Through the examination of single point responses at the center of the perforated plate, the frequency-amplitude relationship is presented and used for model updating. This work showed that linear updating alone is insufficient to assure that a FEM is tuned to correctly capture the nonlinear response. However, when the NNM was measured and used in the updating process it was possible to obtain good agreement. For the nominally flat plate, the fundamental natural frequency of the final updated model is still outside acceptable frequency error ranges; however, there is gained insight to the final stress distribution at increasing amplitudes of response pointing to a more optimal design. The curved plates agree well throughout the updating process, and final stress distributions point to a potential mechanism of the observed experimental failures. This work has shown the benefit of using NNMs to characterize nonlinear behavior and guide model updating for geometrically nonlinear structures. Additional emphasis is placed on the importance of accounting for potential uncertainties in the experiment before changing nonlinear characteristics to obtain a more complete picture of how the structure behaves nonlinearly.

Acknowledgments

Support for this research was provided by the Engineering and Physical Sciences Research Council, the University of Wisconsin – Madison Graduate School with funding from the Wisconsin Alumni Research Foundation and through the Structural Sciences Center in the Air Force Research Laboratory's summer internship program.

References

[1] D.J. Ewins, Modal Analysis Theory, Practice, and Application, Second Edition ed., Research Studies Press Ltd., 2000.
[2] M.I. Friswell, and Mottershead, J.E., Finite Element Model Updating in Structural Dynamics, Kluwer Academic Publishers, 1995.
[3] G.F. Lang, Matrix Madness and Complex Confusion... A Review of Complex Modes from Multiple Viewpoints, Journal of Sound and Vibration, 46 (2012).
[4] R.M. Rosenberg, Normal Modes of Nonlinear Dual-Mode Systems, Journal of Applied Mechanics, 27 (1960) 263-268.
[5] S.W. Shaw, An Invariant Manifold Approach to Nonlinear Normal Modes of Oscillation, Journal of Nonlinear Science, 4 (1994) 419-448.
[6] G. Kerschen, M. Peeters, J.C. Golinval, A.F. Vakakis, Nonlinear normal modes, Part I: A useful framework for the structural dynamicist, Mechanical Systems and Signal Processing, 23 (2009) 170-194.
[7] A.F. Vakakis, Manevitch, L.I., Mikhlin, Y.V., Pilipchuk, V.M., and Zeven, A.A., Normal Modes and Localization in Nonlinear Systems, John Wiley & Sons, New York, 1996.
[8] M. Peeters, Viguie, R., Serandour, G., Kerschen, G., and Golinval, J.C., Nonlinear Normal Modes, Part II: Toward a Practical Computation using Numerical Continuation Techniques, Mechanical Systems and Signal Processing, 23 (2009) 195-216.
[9] N. Boivin, Pierre, C., and Shaw, S., Non-Linear Modal Analysis of Structural Systems using Multi-Mode Invariant Manifolds, in: Dynamics Specialists Conference, Hilton Head, South Carolina, 1994.
[10] M.E. King, Vakakis, A.F., An Energy-Based Approach to Computing Resonant Nonlinear Normal Modes, Journal of Applied Mechanics, 63 (1996) 810-819.
[11] A.H. Nayfeh, Lacarbonara, W., and Chin, C.M., Nonlinear Normal Modes of Buckled Beams: Three-to-One and One-to-One Internal Resonances, Nonlinear Dynamics, 18 (1999) 253-273.
[12] D. Jiang, Pierre, C., and Shaw, S.W.,, The Construction of Non-Linear Normal Modes for Systems with Internal Resonance, International Journal for Nonlinear Mechanics, 40 (2005) 729-746.
[13] T.P. Sapsis, D.D. Quinn, A.F. Vakakis, L.A. Bergman, Effective stiffening and damping enhancement of structures with strongly nonlinear local attachments, Journal of Vibration and Acoustics, Transactions of the ASME, 134 (2012).
[14] D.A. Ehrhardt, Neild, S.A., and Cooper, J.E.,, Experimental and Numerical Investigation of the Nonlinear Bending-Torsion Coupling of a Clamped-Clamped Beam with Centre Masses, in: International Modal Analysis Conference XXXIV, Orlando, FL, 2016.
[15] R.J. Kuether, and Allen, M.S., Computing Nonlinear Normal Modes Using Numerical Continuation and Force Appropriation, in: 24th Conference on Mechanical Vibration and Noise, 2012, pp. 329-340.
[16] R.J. Kuether, B. Deaner, M.S. Allen, J.J. Hollkamp, Evaluation of Geometrically Nonlinear Reduced Order Models with Nonlinear Normal Modes, AIAA Journal, Submitted August (2014).
[17] M. Kurt, Eriten, M., McFarland, D.M., Bergman, L.A., and Vakakis, A.F.,, Metholodology for Model Updating of Mechanical Components with Local Nonlinearities, Journal of Sound and Vibration, 357 (2015).
[18] M. Peeters, G. Kerschen, J.C. Golinval, Dynamic testing of nonlinear vibrating structures using nonlinear normal modes, Journal of Sound and Vibration, 330 (2011) 486-509.
[19] M. Peeters, G. Kerschen, J.C. Golinval, Modal testing of nonlinear vibrating structures based on nonlinear normal modes: Experimental demonstration, Mechanical Systems and Signal Processing, 25 (2011) 1227-1247.
[20] M. Peeters, G. Kerschen, J.C. Golinval, C. Stéphan, P. Lubrina, Nonlinear Normal Modes of a Full-Scale Aircraft, in: T. Proulx (Ed.) Modal Analysis Topics, Volume 3, Springer New York, 2011, pp. 223-242.
[21] A.H. Nayfeh, Introduction to Perturbation Techniques, Wiley, New York, 1981.
[22] W. Lacarbonara, Rega, G., Nayfeh, A.H., Resonant Nonlinear Normal Modes Part I: Analytical Treatment for Structural One-dimensional Systems, International Journal for Nonlinear Mechanics, 38 (2003) 851-872.
[23] S.A. Neild, Cammarano, A., and Wagg, D.J.,, Towards a Technique for Nonlinear Modal Analysis, in: ASME International Design Engineering Technical Conferences and Computers and Information in Engineering Conference, 2012.

[24] A.H. Nayfeh, Nonlinear Oscillations, John Wiley and Sons, New York, 1979.
[25] R.J. Kuether, and Allen, M.S., A numerical approach to directly compute nonlinear normal modes of geometrically nonlinear finite element models, Mechanical Systems and Signal Processing, 46 (2014) 1-15.
[26] R.J. Kuether, Deaner, B.J., Hollkamp, J.J., and Allen, M.S., Evaluation of Geometrically Nonlinear Reduced-Order Models with Nonlinear Normal Modes, AIAA Journal, 53 (2015) 3273-3285.
[27] J.P. Noel, Renson, L., Grappasonni, C., and Kerschen, G., Identification of Nonlinear Normal Modes of Engineering Structures under Broadband Forcing, Mechanical Systems and Signal Processing, 74 (2016) 95-110.
[28] J.M. Londono, Neild, S.A., and Cooper, J.E., Identfication of Backbone Curves of Nonlinear Systems from Resonance Decay Responses, Journal of Sound and Vibration, 348 (2015).
[29] J.M. Londono, Neild, S.A., and Cooper, J.E., An Approach for the Compensation of Resonant Decays in the Identification of Nonlinear Structures, in: International Modal Analysis Conference XXXIV, Orlando, FL, 2016.
[30] A.H. Nayfeh, Nonlinear Interactions: Analytical, Computational, and Experimental Methods, New Your, NY, 2000.
[31] K. Worden, and Tomlinson, G.R., Nonlinearity in Structural Dynamics: Detection, Identification, and Modeling, Institute of Physics Publishing, Bristol and Philadelphia, 2001.
[32] W.S. Rasband, ImageJ, U.S. National Institutes of Health, in, Bethesda, Maryland, USA, 1997-2015.
[33] M.J. Jhung, and Jo, J.C., Equivalent Material Properties of Perforated Plate with Triangular or Square Penetration Pattern for Dynamic Analysis, Nuclear Engineering and Technology, 38 (2006).
[34] R.W. Gordon, J.J. Hollkamp, Reduced-order Models for Acoustic Response Prediction, in, Air Force Research Laboratory, Dayton, OH, 2011.
[35] J.J. Hollkamp, R.W. Gordon, Reduced-order models for nonlinear response prediction: Implicit condensation and expansion, Journal of Sound and Vibration, 318 (2008) 1139-1153.
[36] J.J. Hollkamp, R.W. Gordon, S.M. Spottswood, Nonlinear modal models for sonic fatigue response prediction: a comparison of methods, Journal of Sound and Vibration, 284 (2005) 1145-1163.
[37] R.J. Allemang, The Modal Assurance Criterion (MAC): Twenty Years of Use and Abuse, in: XX International Modal Analysis Conference, Los Angeles, CA, 2002.
[38] D.A. Ehrhardt, Allen, M.S., Yang, S., and Beberniss, T.J.,, Full-Field Linear and Nonlinear Measurements using Continuous-Scan Laser Doppler Vibrometry and High Speed Three-Dimensional Digital Image Correlation, Mechanical Systems and Signal Processing, (2015).
[39] C. Touze, Thomas, O., and Chaigne, A., Hardening/softening behaviour in non-linear oscillations of structural systems using non-linear normal modes, Journal of Sound and Vibration, 273 (2004) 77-101.
[40] W.C. Young, and Budynas, R.G., Roark's Formulas for Stress and Strain, McGraw-Hill Companies, Inc., New York, NY, 2002.